A Ray Optics Framework
for the
Computation of The Sieve Effect Factor for Blood

by

Lesley Northam

A thesis

presented to the University of Waterloo

in fulfillment of the

thesis requirement for the degree of

Master of Mathematics

in

Computer Science

Waterloo, Ontario, Canada, 2010

I hereby declare that I am the sole author of this thesis. This is a true copy of the thesis, including any required formal revisions, as accepted by my examiners.

I understand that my thesis may be made electronically available to the public.

Abstract

Light may traverse a turbid material, such as blood, without encountering any of its pigment particles, a phenomenon known as sieve effect. This phenomenon may result in a decrease in the amount of light absorbed by the material. Accordingly, the corresponding sieve factor needs to be accounted for in optical investigations aimed at the derivation of blood biophysical properties from light transmittance measurements. The existing procedures used for its estimation either lack the flexibility required for practical applications or are based on general formulas that incorporate other light and matter interaction phenomena. In this thesis, a ray optics framework is proposed to estimate the sieve factor for blood samples using a first principles approach. It consists in applying ray-casting techniques to determine the probability that light can traverse a blood sample without encountering any of the pigment (hemoglobin) containing cells. The thickness of the samples as well as the distribution, orientation and shape of the red blood cells are taken into account by the simulation algorithm employed in this framework. The predictive capabilities of the proposed approach are demonstrated through a series of *in silico* experiments. Its effectiveness is further illustrated by visualizations depicting the different blood parameterizations considered in the simulations.

Acknowledgments

I would like to thank my advisor, Prof. Gladimir Baranoski for his guidance and patience. I would like to express gratitude to my thesis readers Prof. Paulo Alencar and Prof. Jeff Orchard. Additionally, I would like to thank Francis Chen and Brad Kimmel for their assistance.

Lastly, I would like to thank my fiancée, Joe Istead for all his help and support over the years.

Contents

List of Figures

List of Tables

List of Symbols

Chapter 1

Introduction

The understanding of the optical properties of blood is essential for a wide range of biomedical applications, from the assessment of hemoglobin concentration and oxygenation levels [2] to the measurement and interpretation of photobiophysical responses of tissues, such as human skin [1], characterized by the presence of this fundamental biological fluid. Accordingly, the investigation of light interactions with blood has always been one of the focal points of biomedical optics research [47]. In the last decades, computer simulations or *in silico* experiments, paired with traditional "wet" experiments, are increasingly being employed in these investigations. The information derived from these simulations, in turn, is being used to support the noninvasive measurement of tissue optical properties required for the diagnosis [44] and treatment of diseases [41].

One of the main components of these *in silico* investigations refers to the modeling of light absorption by organic pigments or absorbers, such as hemoglobin, in order to derive biophysical properties through inversion procedures [38, 7, 23]. The pigments' absorption spectra used in this task are usually obtained under *in vitro* conditions, *i.e.*, their extinction coefficients are computed using light transmission measurements performed in homogeneous solutions in which these pigments (or chromophores) are uniformly distributed [13]. However, in their native (*in situ*) state, natural pigments (*e.g.,* hemoglobin and chlorophyll)

are found in cells or organelles. As a result, when light traverses the material, refractive index differences between cell walls and intercellular medium may cause multiple internal reflections that increase the light optical pathlength, which, in turn, increases the probability of light absorption. This lengthening of the optical pathlength is referred to as the detour effect [9]. To account for changes in the lengthening of the optical pathlength under *in situ* conditions when using *in vitro* absorption (or extinction) curves, several researchers choose to employ a parameter, known as the differential pathlength factor [11, 25], to scale these curves.

The distribution of absorbers within a target material can also have an opposite effect on the light absorption. More specifically, light traversing the material may not encounter any of its absorbers, a phenomenon known as sieve effect [33], which reduces the probability of light absorption. It has been well documented [35, 16, 6] that detour and sieve effects not only have opposite influences in the absorption profile of turbid materials, but they are also more pronounced in different regions of the light spectrum. While a higher or increased rise in absorption values caused by the detour effect is more noticeable in bands of absorption minima [17], the lower or decreased rise in absorption values caused by the sieve effect is more noticeable in bands of absorption maxima [33]. For this reason, the sieve effect is also known as the absorption flattening effect [12] since the peaks in the absorption spectra of the pigments in their native state are depressed relative to the peaks for a homogeneous solution with the same average pigment concentration [31].

Several formulas have been proposed to estimate a factor that can be used to quantify this effect [12, 31, 15, 35]. However, these formulas usually lack the flexibility to efficiently account for variations in the sieve effect caused by changes in the shape and orientation of the pigment containing structures, and rely on measured values that may be unavailable. McClendon and Fukshansky (1990) suggested that a direct and more accurate estimation of the sieve effect factor of an organic tissue could be possible through a detailed examination of its anatomy. To the best of our knowledge, however, such a direct approach has not

been yet presented in the biomedical literature.

In this thesis, we propose a novel ray optics framework for the computation of the sieve effect factor for blood samples. It overcomes the practical constraints of previous methods by using a first principles approach, which consists in geometrically modeling the main pigment containing structures, namely the red blood cells (RBCs) or erythrocytes, and applying ray-casting techniques to compute the probability of a light ray intersecting these cells as it traverses a blood sample. A more realistic three dimensional representation for the biconcave disk shaped red blood cells is proposed in order to increase the accuracy of the computations. We remark that these cells are the primary absorbers and scatterers within whole blood [42], and they are largely responsible for its optical behavior [24, 28]. We computed the sieve effect factor for several blood samples with varying thickness and hematocrit (percentage of blood volume occupied by red blood cells) using the proposed framework to demonstrate its predictability and effectiveness. In addition, we employed different cell shapes and orientations in our *in silico* experiments to illustrate the dependence of sieve effect factors on the geometry and distribution of the erythrocytes.

The remainder of this thesis is organized as follows. Chapter 2 gives necessary biophysical background information on blood and discusses previous work related to the estimation and computation of the sieve effect factor. Chapter 3 describes the algorithm of our proposed sieve effect factor estimation framework. Chapter 4 presents experimental results of the proposed framework. Finally, the thesis concludes in Chapter 5 with a summary of contributions and directions for future work.

Chapter 2

Biophysical Background

2.1　Blood

Blood is essential to human life. It transports oxygen and nutrients to tissues, plays a role in the immune system, and aids in homeostasis[1]. Blood is composed of "formed elements" (a combination of cells and cell particles), and plasma (a straw-coloured saline solution) [29, 39, 5].

2.1.1　Formed Elements

Formed elements, namely erythrocytes, leukocytes, and thrombocytes, compose 45% of blood [29]. Erythrocytes or red blood cells are the most abundant of these elements. Per cubic millimeter, as many as 6.5 million erythrocytes are present in blood [39].

Healthy erythrocytes can be described as biconcave disks (pinched spheres) [47]. They aid in respiration by carrying oxygen through the blood stream [39, 29]. Oxygen permeates red blood cells and binds with hemoglobin, and it is hemoglobin which gives blood its red colour.

Leukocytes, also known as white blood cells, are the least abundant element. Per cubic

---

[1]Homeostasis is a term used to describe the tendency of an organism to maintain a condition of equillibrium. For example, the body's ability to maintain a constant temperature and pH [29, 39, 5].

millimeter as few as 9000 cells may be present in blood [29]. Leukocyte describes a group of cells (eosinophils, basophils, neutrophils, monocytes and lymphocytes) [29]. As a group, leukocytes are responsible for finding infectious organisms (e.g., bacteria, fungus, etc), then destroying them a process known as phagocytosis [5].

Thrombocytes or platelets are not true cells but fragments of cells from bone marrow[2]. Per cubic millimeter approximately 360 thousand may be present in blood [29]. Platelets aid in blood clotting and the formation of scabs[3].

2.1.2   Plasma

Plasma composes 55% of blood [29]. It is a nutrient-rich saline solution that consists of water (90%), proteins (10%), salts, carbohydrates, amino acids, vitamins and hormones [29]. Plasma maintains the electrolyte-fluid balance and pH, and transports nutrients, gasses and vitamins.

2.1.3   Hemoglobin

Hemoglobin is contained within erythrocytes at an average concentration of $319 - 411 g/L$ [47]. It is a conjugated protein formed by four globin proteins and four chromophore molecules of heme [39]. The chromophore heme is red, resulting from an Fe^{2+} cation which is capable of binding oxygen. Ninety-eight percent of oxygen carried by blood is bound to hemoglobin within erythrocytes [39].

---

[2]Bone marrow is the soft tissue found inside bones that produces red blood cells.
[3]A scab is the crust that forms over a wound to protect and aid in healing.

2.2 Optical Background

The transmittance of light traversing a homogeneous solution at a wavelength λ can be obtained using the Beer-Lambert law [16]:

$$T(\lambda) = \frac{\Phi_t(\lambda)}{\Phi_i(\lambda)} = e^{-\varepsilon(\lambda)cd}, \tag{2.1}$$

where Φ_t/Φ_i corresponds to the ratio of incident to transmitted flux, ε and c are the extinction coefficient and the concentration (g/L) of the absorbing substance (pigment) respectively, and d is the optical pathlength through the sample.

The absorptance or optical density[4] of such a solution can be obtained by solving Equation 2.1:

$$D(\lambda) = \ln\left(\frac{\Phi_i(\lambda)}{\Phi_t(\lambda)}\right) = \varepsilon(\lambda)cd. \tag{2.2}$$

In order to compute the optical density of a turbid material such as blood, one can employ a modified version of the Beer-Lambert law:

$$D(\lambda) = \ln\left(\frac{\Phi_i(\lambda)}{\Phi_t(\lambda)}\right) = \beta(\lambda)\varepsilon(\lambda)cd, \tag{2.3}$$

where β corresponds to a scale factor to account for sieve and detour effects.

The scale factor denoted by β is called differential pathlength factor in studies involving human tissues [11] and ratio or factor of intensification in studies involving plant tissues [35]. While in the former it is usually associated only to the lengthening of the optical pathlength due to detour effects, in the latter it also includes the influence of possible sieve effects that could decrease light absorption [35]. For completeness, we adopt the latter description in this thesis, *i.e.*, we define β as $\beta_s\beta_d$, where β_d[5] corresponds to the detour factor and β_s[6] corresponds to the sieve factor, the main focus of this investigation. It is

---

[4]Absorptance or optical density is a measure of how a material transmitts light.
[5]$\beta_d \geq 1$
[6]$0 \leq \beta_s \leq 1$

important to note that the detour factor has a wavelength dependence [21] which does not apply to the sieve factor [33]. This is explained by the fact the detour effects can result from interactions of light with the absorbers, while the sieve effects are directly associated to the absence of such interactions (Figure 2.1).
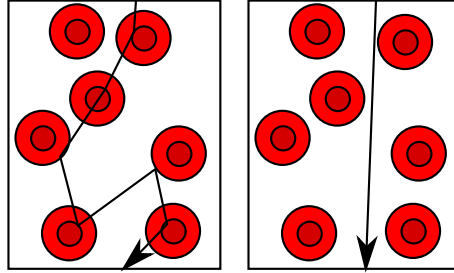
Figure 2.1: Sketches illustrating detour (left) and sieve (right) effects.

2.3 Computing the Sieve Effect

In the literature, several formulas exist for the computation of the sieve factor. For example, Duysens (1956) and Pittman (1986) proposed the following expression:

$$\beta_s = \frac{D_{sus}(\lambda)}{D_{sol}(\lambda)}, \tag{2.4}$$

where D_{sus} and D_{sol} correspond to the optical densities of the pigment in suspension[7] and in solution[8] respectively. If a measured value for D_{sus} is unknown, it is replaced by an approximated value. For example, Duysens (1956) provided approximations for suspensions composed of cubical, spherical and arbitrary shaped particles, and Pittman (1986) provided the following formula to approximate the optical density of red blood cells in suspension and hemoglobin in solution:

$$D_{sus}(\lambda) = m \log_{10} \left[1 - aH(1 - 10^{-\epsilon(\lambda)c_h b}) \right], \tag{2.5}$$

---

[7]When a pigment is contained within a cell or small container distributed throughout a volume, it is referred to as "pigment in suspension".

[8]A homogeneous solution of pigment is referred to as "pigment in solution"

7

and

$$D_{sol}(\lambda) = \epsilon(\lambda)c_h H d, \tag{2.6}$$

where c_h is the concentration of hemoglobin in a red blood cell, H is the hematocrit, a is the cellular shape factor, m is the number of cell layers, and b is the average pathlength through a red blood cell.

Another formula to estimate the sieve effect factor was provided by Fukshansky (1978):

$$\beta_s = \frac{D_{sol}(\lambda) - D_{sus}(\lambda)}{D_{sol}(\lambda)}, \tag{2.7}$$

where

$$D_{sus}(\lambda) = -\ln\left((1-\gamma) + \gamma e^{-\frac{1}{\gamma}D(\lambda)_{sol}}\right), \tag{2.8}$$

and γ corresponds to the fractional area occupied by the pigments containing structures.

We remark that these sieve factor estimation formulas rely on the availability of measured data. Furthermore, the approximations for optical density given in Equations 2.5 and 2.8 do not account for changes in shape, distribution or orientation of the pigment containing structures. Finally, recall that the sieve factor corresponds to the probability that light does not encounter the absorbers, *i.e.*, $0 \leq \beta_s \leq 1$. However, if $D_{\lambda sus} \geq D_{\lambda sol}$ (which may be true for blood [24, 22]), then $\beta_s = D_{sus}(\lambda)/D_{sol}(\lambda) \geq 1$. This indicates that the estimation provided by Equation 2.4 may also include the detour effect. Similar observations with respect to other natural pigments (*e.g.*, chlorophyll) have been reported in the literature [35]. In the proposed framework, which is described in the following section, the limitations outlined above are addressed through the application of a first principles approach.

Chapter 3

Experimental Materials and Methods

The proposed framework combines ray optics concepts with ray casting techniques to obtain an estimate for the sieve effect factor of blood samples contained in a testing volume. In this section, we describe the general algorithm and blood-specific parameterizations used in our simulations, and outline relevant implementation issues.

3.1   General Algorithm

Our framework operates on the idea of generating a geometrical blood sample and a ray, then testing for intersections between sample blood cells and the ray.

A Monte Carlo based algorithm is employed in our *in silico* experiments, and its basic steps are summarized as follows:

1. initialize no-hits counter $n = 0$

2. generate and randomly distribute cells within the test volume according to user-specified parameters defining the experimental conditions

3. compute the number of cells intersecting a ray sent through the volume

4. if no cells are intersected by the ray, increment n

5. repeat steps 1-4 N times

6. compute sieve factor $\beta_s = n/N$

The ray-cell intersection procedures employed in this thesis are outlined in Appendix A.

3.2 Testing Volume

Volume size affects algorithm performance since cell count is proportional to volume. For example, a $1.0mm^3$ sample of human blood contains five million red blood cells (47% hematocrit) [47]. It would be impractical to consider such a volume since 5×10^6 ray-cell intersection tests would be required per iteration. Hence, to reduce cell count, we selected a rectangular prism volume with dimensions given by $0.1mm \times 0.1mm \times t$, where t corresponds to the blood sample thickness.

3.3 Cell Geometry

Although red blood cells (RBC) resemble biconcave disks [47], they are usually approximated by simpler shapes like volume or surface area equivalent spheres [47, 42]. In our *in silico* experiments, we employed a closer approximation to the RBCs. It consists in the union of a torus with a cylinder, herein referred to as a TUC-cell (Figure 3.1). It is important to note that not all erythrocytes have exactly the same shape, and small deviations from the standard biconcave disk shape are expected specially due to micro and macro environmental changes. For example, during certain flow conditions [40], these cells change into a parachute like shape without large variations in their overall length or forward end during acceleration from rest. To the best of our knowledge, however, data quantitatively describing these shape deviations is not readily available in the literature. Hence, for the purpose of this investigation, it is assumed that all cells have the same shape, and the
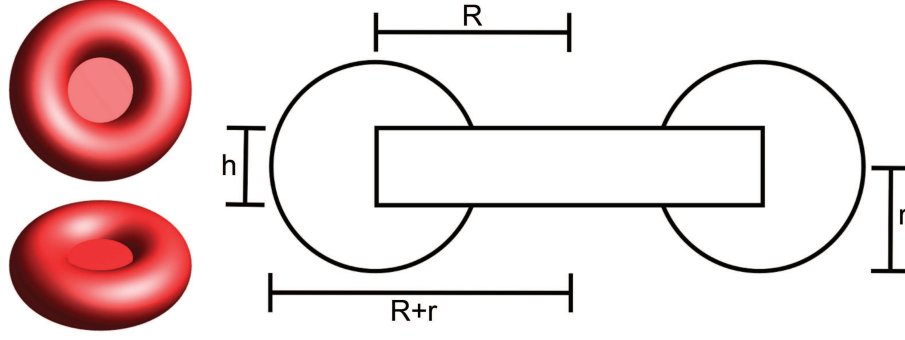
Figure 3.1: Dimensions of a TUC-cell. On the left, raytraced views of the final shape. On the right, a cross-section of the TUC-cell showing the dimensions of the torus and cylinder. Cylinder has radius $R = 2.62\mu m$, and height $h = 0.81\mu m$. Torus has major radius $R = 2.62\mu m$, and minor radius $r = 1.29\mu m$ (diameter $2r = 2.58\mu m$). The radius of the TUC-cell is given by $R + r = 3.91\mu m$.

propagation of light through the samples is perfomed under steady-state environmental conditions.

The volume of a TUC-cell was computed taking into account the geometry described in Figure 3.1, and considering the volume of the torus added to a volume of revolution defined by the volume of the cylinder not inside the torus. Derivation details are provided in Appendix B. The resulting expression is given by:

$$V_{TUC} = 2\pi^2 R r^2 + 2\pi \left[r R^2 \sin x - r^2 R \left(\frac{1}{2}x + \frac{1}{4}\sin(2x) \right) + r^3 \left(\frac{1}{3}(2 + \cos^2 x)\sin x \right) \right], \tag{3.1}$$

where

$$x = \sin^{-1}\left(\frac{h/2}{r} \right). \tag{3.2}$$

The dimensions of a TUC-cell, given by $r = 1.29\mu m$, $R = 2.62\mu m$ and $h = 0.81\mu m$, were selected according to physiological limits provided in the literature [47]. As a result, the volume computed for the TUC-cell ($90.7\mu m^3$) using Equation 3.1 is within the physiological range provided for the volume of an actual red blood cell, namely $94 \pm 14\mu m^3$ [47, 42].

3.4 Generation and Distribution of TUC-Cells

Given the testing volume (V_{prism}) and hematocrit (H), the number of TUC-cells (K) to be generated is computed using:

$$K = H\frac{V_{prism}}{V_{TUC}}. \tag{3.3}$$

The generated TUC-cells are randomly distributed throughout the volume obeying the following rules:

1. a TUC-cell must exist entirely within the volume, and

2. TUC-cells cannot overlap.

Collision detection is performed for each TUC-cell prior to placement, preventing overlaps. This operation is simplified by encompassing each cell in a bounding volume, and then testing for intersections between bounding volumes. After the TUC-cells are distributed, their bounding volumes are removed and play no part in the actual computation of the sieve factor.

The procedure employed for collision detection has two main phases. Phase 1 tests for collision between bounding spheres (with radius $R + r$). If a collision between bounding spheres is detected, then phase 2 is executed. In phase 2, collision detection is performed using a bounding shape for the TUC-cell, henceforth referred to as "sphere pack" (Figure 3.2). Implementation details are provided in Appendix C. This shape was selected due its higher accuracy and cost ratios (compared to cylinders or torii) with respect to collision computations. The sphere pack consists of three circular planes or "plates" (top, middle and bottom with radii equal to R, $R + r$ and R respectively), and a ring of spheres (with radius r).
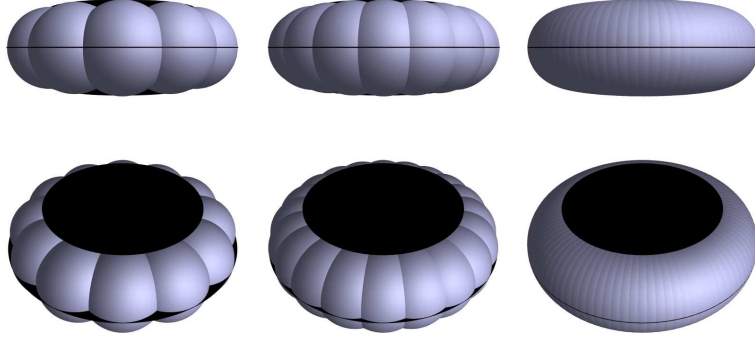
Figure 3.2: Images describing the "sphere pack" bounding shape used to detect collisions between TUC-cells. On the left, 12 spheres are used; in the middle, 20 spheres; and on the right, 100 spheres. Top and bottom images represent the same object viewed from different angles. Note that by increasing the number of spheres forming the ring, the smoother the bounding shape becomes. However, increasing sphere count decreases the performance of the collision detection procedure.

3.5   Implementation Issues

The stochastic nature of the proposed simulation algorithm requires a large numbers of iterations, *i.e.*, N has to be large enough to guarantee asymptotically convergent results. In our experiments, we used $N = 10^5$.   Hence, the estimation of the sieve factor may become computationally expensive. However, the algorithm iterations are independent (Section 3.1), and therefore parallelizable. Accordingly, we implemented the proposed algorithm on the CUDA platform [10], a massively multi-threaded computational environment in which thousands of ray-cell intersection tests can be done in parallel. Implementation details are provided in Appendix D.

We also generated images to further illustrate our *in silico* experiments and to broaden the analysis of their results. These images were rendered using the open-source ray-tracing simulation package "POV-Ray 3.6" [30].

3.6   Experimental Setup

Three sets of experiments were conducted. In each set, a different sample thickness ($0.1mm$, $0.25mm$ and $1.0mm$) was adopted, and three representations for the erythrocytes, namely

volume equivalent spheres, randomly oriented TUC-cells (simulating agitated blood) and flow oriented TUC-cells, were used to compute the sieve factor for samples with hematocrits varying between 1% and 10%. The values selected for these experimental parameters are consistent with blood optical investigations described in the literature (Table 3.1).

Table 3.1: Summary of biophysical parameters employed to describe the different *in silico* experimental conditions considered in this investigation.

Parameter	Default Value	Range	Source
Sample Thickness	$0.1mm$	$0.1mm$–$1.0mm$	[42, 3, 4, 27, 48, 14, 18]
Hematocrit	5%	1–10%	[42, 14, 18, 34, 27]
Orientation	random	random, flow	[40, 32]

The light incidence direction is assumed to be perpendicular to the top face of testing volume[1], *i.e.*, it is parallel to the main axis of the flow oriented TUC-cells[2]. It is important to note that a flow oriented TUC-cell is characterized by having the plane containing its main axis perpendicular to the flow direction [32, 40]. We remark that this orientation only affects TUC-cells since volume equivalent spheres are symmetrical.

---

[1]Light enters at the top, and exits at the bottom of the testing volume.
[2]The main axis of a flow-oriented TUC-cell is the axis of largest radius.

Chapter 4

Results

An increase in the number of erythrocytes decreases the amount of unoccupied space within the volume of blood sample, which, in turn, increases the probability of light intersecting these cells. Hence, the sieve factor is expected to decrease as hematocrit increases [31]. As can be observed in the plots presented in Figures 4.1 to 4.3, the results provided by the proposed framework are consistent with this trend.

Similarly, the sieve factor is expected to be higher for volume equivalent spheres because their surface area and profile are smaller than those of a TUC-cell. Visually, a cell profile corresponds to the area occupied by a cell when projected onto a plane, *i.e.*, the area of an orthographically projected TUC-cell lying flat on a table is larger than the area of an orthographically projected volume equivalent sphere. As can be observed in the plots depicted in Figures 4.1 to 4.3 the results provided by the proposed framework are also consistent with this trend.

It has long been determined that the sieve effect is smaller when the absorbers have an uniform (parallel) random distribution with respect to the light incidence direction [33]. Accordingly, the sieve factor is expected to be higher for flow oriented TUC-cells in comparison with randomly oriented (agitated) TUC-cells. As it can be observed in the plots presented in Figures 4.1 to 4.3, the results provided by proposed framework agree
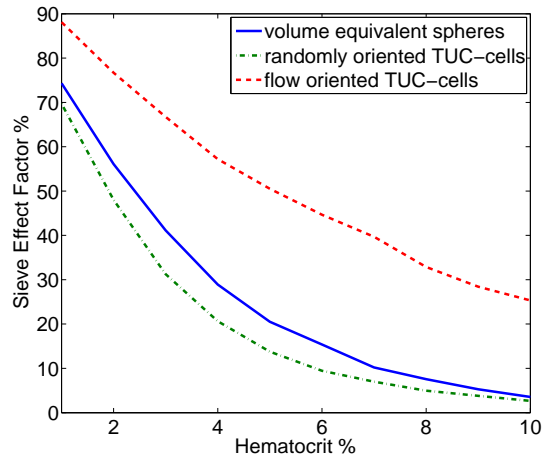
Figure 4.1: Plots of sieve effect factors computed for blood samples with thickness equal to 0.1mm. Three representation for the erythrocites were considered in these experiments: volume equivalent spheres, randomly oriented TUC-cells and flow oriented TUC-cells.
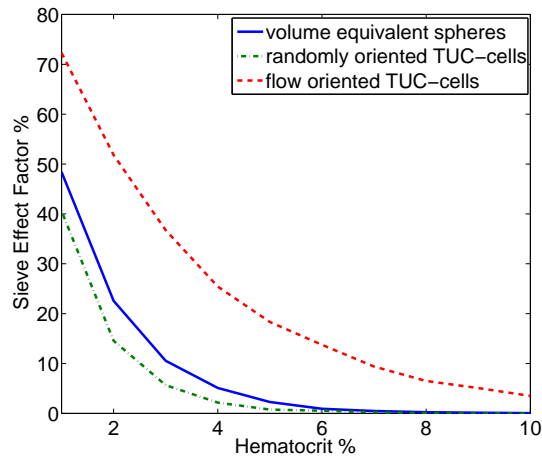
Figure 4.2: Plots of sieve effect factors computed for blood samples with thickness equal to 0.5mm. Three representation for the erythrocites were considered in these experiments: volume equivalent spheres, randomly oriented TUC-cells and flow oriented TUC-cells.
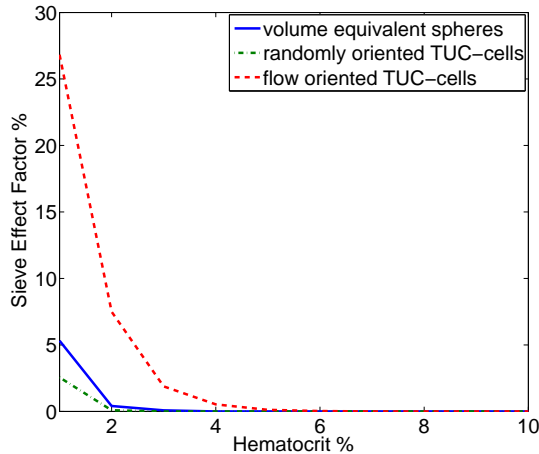
Figure 4.3: Plots of sieve effect factors computed for blood samples with thickness equal to 1.0*mm*. Three representation for the erythrocites were considered in these experiments: volume equivalent spheres, randomly oriented TUC-cells and flow oriented TUC-cells.

with this expectation. This difference can be visualized in the simulation images provided in Figure 4.4. Note the increased visibility of the face below the blood cells (which is perpendicular to the light incidence direction) in a flow orientation in comparison with a random orientation. The increased visibility resulting from a flow orientation is associated to a higher sieve effect factor, *i.e.*, a higher probability of light traversing the sample without encountering any of the erythrocytes.

In order to extend our scope of observations, we also generated images depicting the different cell geometries taken into account in our *silico* experiments. As it can be observed in the images presented in Figure 4.5, volume equivalent spheres occupy less cross-sectional area than randomly oriented TUC-cells. Moreover, these images show how an increase in hematocrit affects the cell count and distribution. More specifically, the increase in hematocrit increases cell count, and reduces the visibility of the face below the blood sample.

It has been suggested in the literature [16] that the sieve effect is independent of the sample thickness. In fact, if one replaces d by t in Equation 2.2, t can be eliminated from Equations 2.4 and 2.7. We remark, however, that such estimations may incorporate both
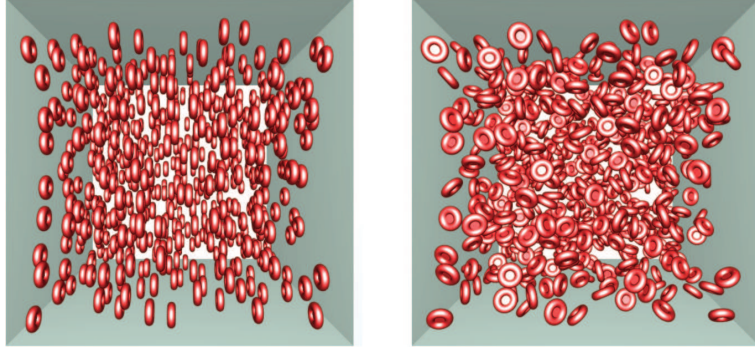
Figure 4.4: Images illustrating different TUC-cell profiles as observed from viewing direction coincident with the light incidence direction. Left: flow oriented TUC-cells. Right: randomly oriented TUC-cells. These images correspond to simulations involving samples with a thickness equal to $0.1mm$ and hematocrit equal to 5%. Note the amount of space each appears to take looking down into the volume.

sieve and detour effects [35, 26]. As can be observed in the images presented in Figure 4.6, the visibility of the face below the blood sample is reduced when the sample thickness is increased and the hematocrit is kept constant. These visual simulations intuitively demonstrate that the probability of light traversing the medium without encountering the erythrocytes is reduced under these conditions, *i.e.*, the sieve effects decrease as the sample thickness is increased.

Supplementary results related to the implementation of proposed framework are presented in Appendix E.

4.1 Limitation

Through experimentation, a limitation in the proposed framework was discovered. Let's assume N cells have been distributed within the volume. It is possible that even though there is enough volume space, the next cell cannot be inserted due to the fact that this space is fragmented by the distribution of the N cells. When this occurs, the algorithm loops (until stopping criteria is met) because no valid (collision free) position for cell $N+1$ can be found.

The experimental results presented in this thesis were not affected by this limitation
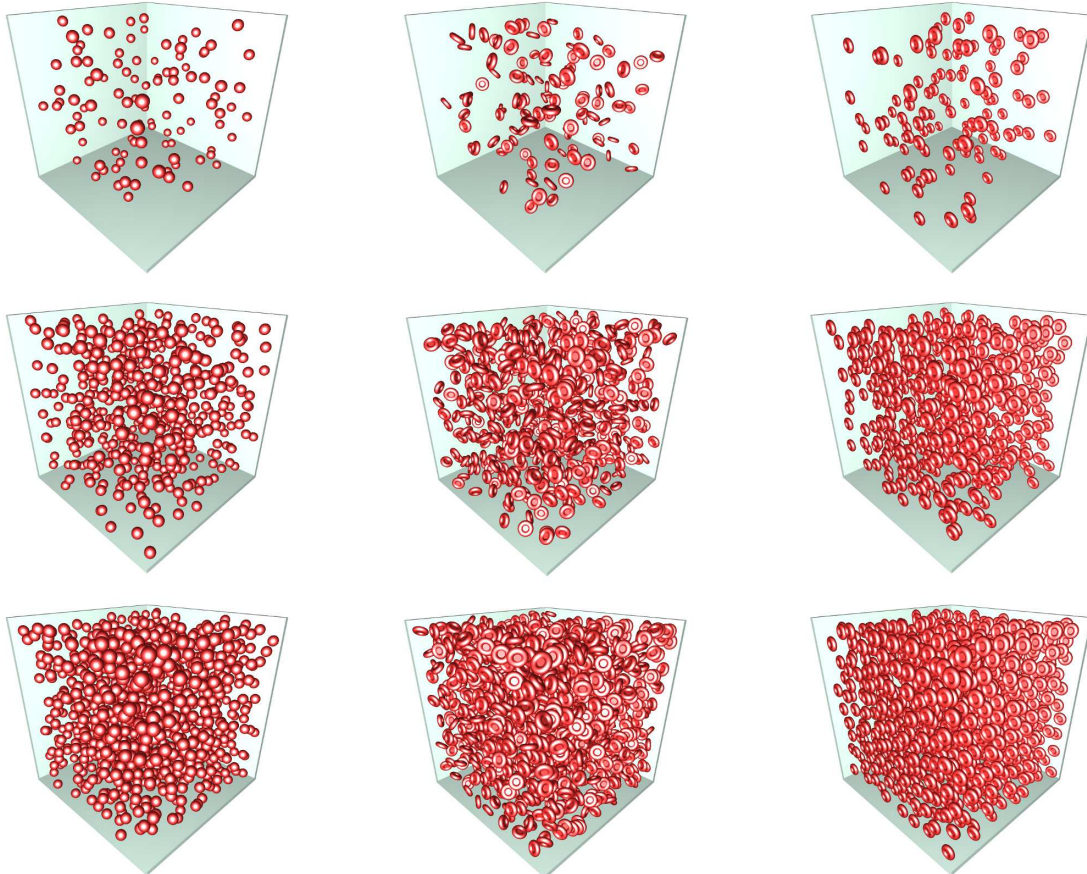
Figure 4.5: Images illustrating the different blood geometries considered in the computation of the sieve effect factor. Left column: volume-equivalent spheres. Middle column: randomly-oriented TUC-cells. Right column: flow-oriented TUC-cells. Hematocrit of top row is 1%; middle row, 5%; and bottom row, 10%. These images correspond to simulations involving samples with a thickness equal to $0.1mm$ and assuming the light incidence direction to be perpendicular to the top face of the testing volume, which was removed to facilitate the visualization of the testing (sample) volume.
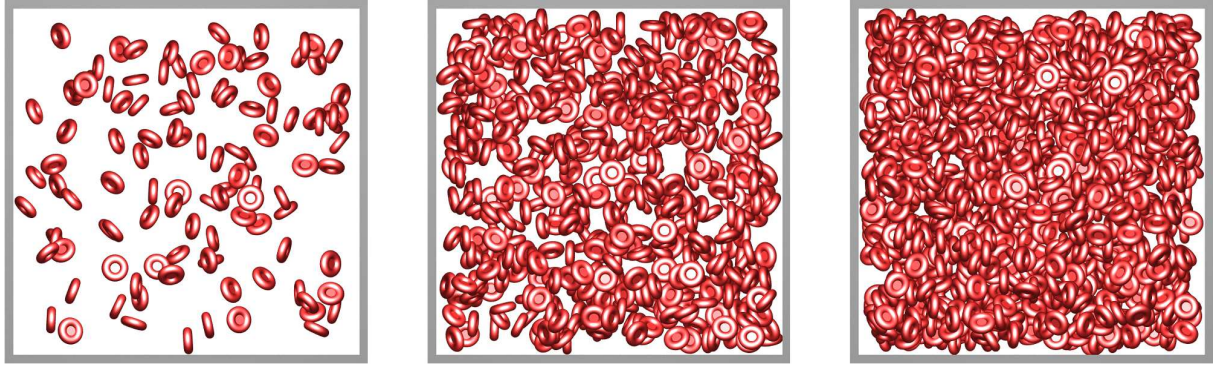
Figure 4.6: Ortographic projections (perpendicular to the light incidence direction) of three blood samples with different thicknesses and the same hematocrit (1%). Left: $0.1mm$. Middle: $0.5mm$. Right: $1.0mm$.

because their hematocrit values (and therefore cell count) are sufficiently low. Increasing hematocrit beyond 10% increases the probability of encountering this limitation. However, this only presents an issue when sample thickness is thin and resulting sieve effect is greater than zero at $H = 10\%$. For example, this limitation occurs when we attempt to compute sieve effect for a 0.1mm sample considering either randomly-oriented TUC-cells with $H > 10\%$ or flow-oriented TUC-cells with $H > 20\%$. We remark that these thickness and hematocrit values are not routinely employed in blood optical experiments.

Chapter 5

Conclusions

5.1 Contributions

We have presented a ray optics framework to estimate the sieve factor for blood samples. It employs ray-casting techniques to compute the probability that light does not intersect any erythrocyte in a sample simulating the anatomical characteristics of blood. Its predictive capabilities were demonstrated through a series of *in silico* experiments whose results qualitatively agree with observations reported in the literature.

We remark that a predictive *in silico* experimental framework may also be used to accelerate the hypothesis generation and validation cycles of research involving the behavior of biological systems [45]. Accordingly, the results of our investigation have demonstrated that the sieve factor is affected not only by cell shape and orientation, but also by the sample thickness.

5.2 Future Work

The presented simulation framework is generalizable and, therefore, applicable to other natural materials with similar pigment containing structures such as melanosomes (human tissues) and chloroplasts (plant tissues). As future work, we intend to explore this research

avenue and integrate the outcomes of this investigation into comprehensive models of light interaction with organic materials.

As discussed in Section 4.1, the proposed framework encounters a limitation in the generation of cell distrubtions with hematocrits greater than 10%. In our future work, we also intend to explore alternatives to overcome this limitation. Such alternatives may include distribution techniques such as weighted Voronoi diagrams [37], or circuit placement algorithms [20].

Bibliography

[1] AGACHE, P. *Assessment of erythema and pallor.* Springer-Verlag, Berlin, 2004.

[2] AMELINK, A., CHRISTIAANSE, T., AND STERENBORG, H. J. C. M. Effect of hemoglobin extinction spectra on optical spectroscopic measurements of blood oxygen saturation. *Opt. Lett. 34*, 10 (2009), 1525–1527.

[3] ANDERSON, N. M., AND SEKELJ, P. Light-absorbing and scattering properties of nonhaemolysed blood. *Physics in Medicine and Biology 12*, 2 (1967), 173–184.

[4] ANDERSON, N. M., AND SEKELJ, P. Reflection and transmission of light by thin films of nonhaemolysed blood. *Physics in Medicine and Biology 12*, 2 (1967), 185–192.

[5] ARMS, K. *Biology*, 4th ed. Harcourt Brace College Publisher, San Diego, California, 1982.

[6] BARANOSKI, G., AND ENG, D. An investigation on sieve and detour effects affecting the interaction of collimated and diffuse infrared radiation (750 to 2500 nm) with plant leaves. *Geoscience and Remote Sensing, IEEE Transactions on 45*, 8 (2007), 2593–2599.

[7] BARUN, V. V., AND IVANOV, A. P. Effect of hemoglobin localization in erythrocytes on optical absorption by human blood. In *Tenth International Conference on Light Scattering by Non-spherical Particles* (Bodrun, Turkey, 2007), pp. 5–8.

[8] Breen, B. J., Weidert, C. E., Lindner, J. F., Walker, L. M., Kelly, K., and Heidtmann, E. Invitation to embarrassingly parallel computing. *American Journal of Physics 76*, 4 (2008), 347–352.

[9] Butler, W. L. Absorption spectroscopy in vivo: Theory and applications. *Annual Review of Plant Physiology 15* (1964), 451–470.

[10] Chei, S., Boyer, M., Meng, J., Tarjan, D., Sheaffer, J. W., and Skadron, K. A performance study of general-purpose applications on graphics processors using cuda. *J. Parallel Distrib. Comput. 68*, 10 (2008), 1370–1380.

[11] Delpy, D. T., Cope, M., van der Zee, P., Arridge, S., Wray, S., and Wyatt, J. Estimation of optical pathlength through tissue from direct time of flight measurement. *Physics in Medicine and Biology 33*, 12 (1988), 1433–1442.

[12] Duysens, L. N. M. The flattening of the absorption spectrum of suspensions as compared to that of solutions. *Biochimica et Biophysica Acta 19* (1956).

[13] Eng, D., and Baranoski, G. The application of photoacoustic absorption spectral data to the modeling of leaf optical properties in the visible range. *Geoscience and Remote Sensing, IEEE Transactions on 45*, 12 (Dec. 2007), 4077–4086.

[14] Flock, S. T., Wilson, B. C., and Patterson, M. S. Total attenuation coefficient and scattering phase function of tissues and phantom materials at 633nm. *Med. Phys. 14* (1987), 1742–1753.

[15] Fukshansky, L. On the theory of light absorption in non-homogeneous objects. *Journal of Mathematical Biology 6*, 2 (1978), 1416–1432.

[16] Fukshansky, L. *Optical properties of plants.* Academic Press, London, 1981.

[17] Garlaschi, F., Zucchelli, G., and Jennings, R. Studies on light absorption and photochemical activity changes in chloroplast suspensions and leaves due to light

scattering and light filtartion across chloroplasts and vegetation layers. *Photosynthesis Research 20* (1989), 207–220.

[18] HAMMER, M., SCHWEITZER, D., MICHEL, B., THAMM, E., AND KOLB, A. Single scattering by red blood cells. *Appl. Opt. 37*, 31 (1998), 7410–7418.

[19] HEARN, D., AND BAKER, M. P. *Computer Graphics with OpenGL*, 3 ed. Pearson Prentice Hall, Upper Saddle River, NJ, 2004.

[20] KENNINGS, A., AND VORWERK, K. Force-directed methods for generic placement. *Computer-Aided Design of Integrated Circuits and Systems, IEEE Transactions on 25*, 10 (Oct. 2006), 2076–2087.

[21] KOHL, M., NOLTE, C., HEEKEREN, H. R., HORST, S., SCHOLZ, U., OBRIG, H., AND VILLRINGER, A. Determination of the wavelength dependence of the differential pathlength factor from near-infrared pulse signals. *Physics in Medicine and Biology 43*, 6 (1998), 1771–1782.

[22] KRAMER, K., ELAM, J., SAXTON, G., AND JR., W. E. Influence of oxygen saturation, concentration and optical depth upon the red and near-infrared light transmittance of whole blood. *Am. J. Physiology 165* (1951), 229–246.

[23] LAUFER, J., DELPY, D. T., ELWELL, C., AND BEARD, P. Quantitative spatially resolved measurment of tissue chromophore concentrations using photoacoustic spectroscopy: application to the measurement of blood oxygenation and haemoglobin concentration. *Physics in Medicine and Biology 52* (2007), 141–168.

[24] LOVELL, A. T., HEBDEN, J. C., GOLDSTONE, J. C., AND COPE, M. Determination of the transport scattering coefficient of red blood cells [3597-121]. In *Society of Photo-Optical Instrumentation Engineers (SPIE) Conference Series* (Apr. 1999), B. Chance, R. R. Alfano, and B. J. Tromberg, Eds., vol. 3597, p. 175.

[25] MATCHER, S. J., COPE, M., AND DELPY, D. T. Use of the water absorption spectrum to quantify tissue chromophore concentration changes in near-infrared spectroscopy. *Physics in Medicine and Biology 39*, 1 (1994), 177–196.

[26] MCCLENDON, J. H., AND FUKSHANSKY, L. On the interpretation of absorption spectra of leaves - ii. the non-absorbed ray of the sieve effect and the mean optical pathlength in the remainder of the leaf. *Photochemistry and Photobiology 51*, 2 (1990), 211–216.

[27] MEINKE, M., MÜLLER, G., HELFMANN, J., AND FRIEBEL, M. Empirical model functions to calculate hematocrit-dependent optical properties of human blood. *Appl. Opt. 46*, 10 (2007), 1742–1753.

[28] MEINKE, M., MÜLLER, G., HELFMANN, J., AND FRIEBEL, M. Optical properties of platelets and blood plasma and their influence on the optical behavior of whole blood in the visible to near infrared wavelength range. *Journal of Biomedical Optics 12*, 1 (2007), 014024–1–014024–9.

[29] METZLER, D. E. *Biochemistry The Chemical Reactions of Living Cells*, 1 ed., vol. 2. Harcourt/Academic Press, San Diego, California, 2001.

[30] ORF, L. Scientific visualizations with pov-ray. *Linux J. 2004*, 127 (2004), 2.

[31] PITTMAN, R. N. In vivo photometric analysis of hemoglobin. *Annals of Biomedical Engineering 14*, 2 (1986), 1416–1432.

[32] POPOV, E. G. Orientation of nonspherical cells in blood flowing through a vessel. *Bulletin of Experimental Biology and Medicine 86*, 5 (1978), 1556–1557.

[33] RABINOWITCH, E. I. *Light absorption by pigments in the living cell*, vol. II. Interscience Publishers Inc., New York, 1951, ch. 22.

[34] ROGGAN, A., FRIEBEL, M., DOERSHEL, K., HAHN, A., AND MUELLER, G. Optical properties of circulating human blood in the wavelength range 400-2500nm. *Journal of Biomedical Optics 4*, 1 (1999), 36–46.

[35] RÜHLE, W., AND WILD, A. The intensification of absorbance changes in leaves by light dispersion. *Planta 146*, 5 (1979), 551–557.

[36] SCHWARZE, J. *Cubic and Quartic Roots*. Academic Press, Inc., San Diego, CA, 1990.

[37] SECORD, A. Weighted voronoi stippling. In *NPAR '02: Proceedings of the 2nd international symposium on Non-photorealistic animation and rendering* (New York, NY, USA, 2002), ACM, pp. 37–43.

[38] SEREBRENNIKOVA, Y. M., SMITH, J. M., HUFFMAN, D. E., LEPARC, G. F., AND GARCÍA-RUBIO, L. H. Quantitative interpretations of visible-nir reflectance spectra of blood. *Opt. Express 16*, 22 (2008), 18215–18229.

[39] SHERMAN, I. W. *Biology: A Human Approach*, 4th ed. Kendall/Hunt, Iowa, 1989.

[40] SKALAK, R., AND BRANEMARK, P. I. Deformation of Red Blood Cells in Capillaries. *Science 164*, 3880 (1969), 717–719.

[41] STAR, W. M. Light dosimetry in vivo. *Physics in Medicine and Biology 42*, 5 (1997), 763–787.

[42] STEINKE, J. M., AND SHEPHERD, A. P. Comparison of mie theory and the light scattering of red blood cells. *Appl. Opt. 27*, 19 (1988), 4027–4033.

[43] STEWART, J. *Calculus*, 4 ed. Brooks/Cole Publishing Company, New York, 1999.

[44] TUCHIN, V. V. *Tissue Optics Light Scattering Methods and Instruments for Medical Diagnosis*. The International Society for Optical Engineering, Bellingham, 2000.

[45] VENTURA, B. D., LEMERLE, C., MICHALODIMITRAKIS, K., AND SERRANO, L. From *in vivo* to *in silico* biology and back". *Nature 443* (2006), 527–533.

[46] WAGNER, M., AND HANSON, J. Ray/torus intersection. Class Notes: CS400, 2004.

[47] YAROSLAVSKY, A. N., PRIEZZHEV, A. V., RODRIQUEZ, J., YAROSLAVSKY, I. V., AND BATTARBEE, H. *Optics of Blood*. SPIE-Press, Bellingham, 2002.

[48] YAROSLAVSKY, A. N., YAROSLAVSKY, I. V., GOLDBACH, T., AND SCHWARZ-MAIER, H. J. Influence of the scattering phase function approximation on the optical properties of blood determined from the integrating sphere measurements. *Journal of Biomedical Optics 4*, 47 (1999), 47–53.

Index

Appendix A

Ray-Object Intersections

The ray casting framework detailed in this thesis uses three types of ray-object intersections. They are:

1. ray-sphere,

2. ray-circle, and

3. ray-torus.

A.1 Ray-Sphere Intersection

Let S be a sphere with center P and radius r, and let $v = Q + s\vec{u}$ be a ray. Then if v intersects S, the points of intersection are defined by [19]:

$$s = \vec{u} \circ (PQ) \pm \sqrt{(\vec{u} \circ (PQ))^2 - |PQ|^2 + r^2}, \tag{A.1}$$

where $PQ = P - Q$, and $\vec{u} \circ (PQ)$ represents the dot product of vectors $\vec{u}$ and PQ. If there are no roots (no real values for s), then there is no intersection.

A.2 Ray-Circle Intersection

Let C be a circle with center C_c on the plane defined by $\prod : n \circ C_c = d$, and let $v = Q + s\vec{u}$ be a ray. Then if v intersects the plane, the point of intersection is defined by [19]:

$$s = -\frac{d + \vec{n} \circ Q}{\vec{n} \circ \vec{u}}. \tag{A.2}$$

The point defined as $P_0 = Q + s\vec{u}$ represents the intersection of the ray v with the plane. If the point satisfies $x^2 + y^2 \leq r^2$, then the point lies on the circle, thus the ray intersects the circle (assuming the circle is on the xy-plane).

A.3 Ray-Torus Intersection

The equation of a torus on the xy-plane is [19, 46]:

$$(x^2 + y^2 + z^2 - R^2 - r^2)^2 + 4R^2(z^2 - r^2) = 0 \tag{A.3}$$

To determine if a ray $v = Q + s\vec{u}$ intersects the torus, substitute $x = Q_x + s\vec{u}_x$, $y = Q_y + s\vec{u}_y$, and $z = Q_z + s\vec{u}_z$ into (A.3):

$$\left((Q_x + s\vec{u}_x)^2 + (Q_y + s\vec{u}_y)^2 + (Q_z + s\vec{u}_z)^2 - R^2 - r^2\right)^2 + 4R^2\left((Q_z + s\vec{u}_z)^2 - r^2\right). \tag{A.4}$$

Substituting in the dot product where appropriate yields:

$$\left(Q \circ Q + 2sQ \circ \vec{u} + s^2\vec{u} \circ \vec{u} - R^2 - r^2\right)^2 + 4R\left((Q_z + s\vec{u}_z)^2 - r^2\right). \tag{A.5}$$

Then, after simplification an equation in terms of s is found as $A_0 s^4 + A_1 s^3 + A_2 s^2 + A_3 s +$

$A_4 = 0$, where:

$$A_0 = (\vec{u} \circ \vec{u})^2 \tag{A.6}$$

$$A_1 = 4(\vec{u} \circ \vec{u})(Q \circ \vec{u}) \tag{A.7}$$

$$A_2 = 4(Q \circ \vec{u})^2 + 2(\vec{u} \circ \vec{u})((Q \circ Q) - r^2 - R^2) + 4R^2\vec{u}_z^2 \tag{A.8}$$

$$A_3 = 4(Q \circ \vec{u})((Q \circ Q) - r^2 - R^2) + 8R^2Q_z\vec{u}_z \tag{A.9}$$

$$A_4 = ((Q \circ Q) - r^2 - R^2)^2 + 4R^2Q_z^2 - 4R^2r^2. \tag{A.10}$$

An algorithm to solve this quartic system is provided by Schwarze [36]. If there are no roots, then there is no intersection. Otherwise, there may be one, two or four points of intersection.

Appendix B

Derivation of TUC-cell Volume

A TUC-cell is the union of a torus and a cylinder. The radius of the cylinder (R) is the same as the major radius of the torus. Therefore, a portion of the cylinder's volume is contained within the torus. This provides an upper bound for the volume of the TUC-cell:

$$V = 2\pi^2 R r^2 + \pi R^2 h, \tag{B.1}$$

which is the sum of torus and cylinder volumes ($h = 2t$ is the height of the cylinder).

The exact volume of the TUC-cell can be computed by summing the volumes of the torus and the "dented" cylinder formed by the gray area in Figure B.1.

The volume of the dented cylinder is computed by the integrating disks method [43]. Since the cylinder is symetric, we can solve for the half dented cylinder case, then double this volume to find the full cylinder's volume.

Considering $t = h/2$, the volume of a disk is given by: A disk has volume given by:

$$V_{disk} = \pi [w(t)]^2 dt. \tag{B.2}$$
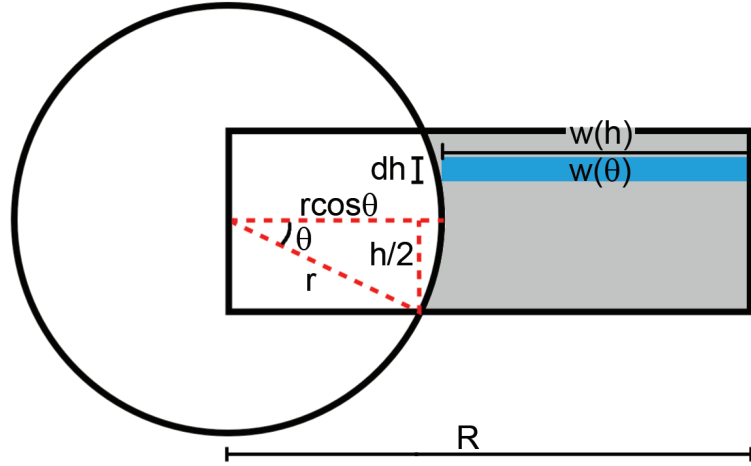
Figure B.1: Dimensions of the dented cylinder.

Hence, the volume of the half dented cylinder is given by:

$$V_{halfcyl} = \pi \int_0^t w(t)^2 dt. \tag{B.3}$$

This can be simplified by integrating over θ instead of t. To do this, a change of variable is performed. Considering the geometry described in Figure B.1, one can obtain:

$$h/2 = t = r\sin\theta \rightarrow \theta = \sin^{-1}\left(\frac{t}{r}\right), \tag{B.4}$$

which corresponds to the upper bound of integration.

Also noting that $w(\theta) = w(t)$ one can obtain:

$$R = w(\theta) + r\cos\theta \rightarrow w(\theta) = R - r\cos\theta. \tag{B.5}$$

Substituting Equations B.4 and B.5 into Equation B.3 yields:

$$V_{halfcyl} = \pi \int_0^{\sin^{-1}\left(\frac{t}{r}\right)} [w(\theta)]^2 dt$$

$$= \pi \int_0^{\sin^{-1}\left(\frac{t}{r}\right)} [R - \cos\theta]^2 dt \tag{B.6}$$

Finally, one can represent dt as:

$$dt = dt\frac{d\theta}{d\theta} = \frac{dt}{d\theta}d\theta = r\cos\theta d\theta. \tag{B.7}$$

Substituting Equation B.7 into Equation B.6 completes the change of variable:

$$\begin{aligned} V_{halfcyl} &= \pi \int_0^{\sin^{-1}\left(\frac{t}{r}\right)} [R - \cos\theta]^2 dt \\ &= \pi \int_0^{\sin^{-1}\left(\frac{t}{r}\right)} [R - \cos\theta]^2 \frac{dt}{d\theta} d\theta \\ &= \pi \int_0^{\sin^{-1}\left(\frac{t}{r}\right)} [R - \cos\theta]^2 (r\cos\theta) d\theta. \end{aligned} \tag{B.8}$$

The volume of the half cylinder (Equation B.8) expands to become:

$$V_{halfcyl} = \pi \int_0^{\sin^{-1}\left(\frac{t}{r}\right)} [R^2 r\cos\theta - 2r^2 R\cos^2\theta + r^3\cos^3\theta] d\theta. \tag{B.9}$$

Therefore, the volume of the TUC-cell is given by:

$$\begin{aligned} V_{TUC} &= V_{torus} + 2V_{halfcyl} \\ &= 2\pi^2 R r^2 + 2\pi \left\{ \int_0^{\sin^{-1}\frac{t}{r}} r R^2\cos\theta - 2r^2 R\cos^2\theta + r^3\cos^3\theta d\theta \right\}. \end{aligned} \tag{B.10}$$

B.1   Computing the Volume of a TUC-cell with Erythrocyte Dimensions

The volume of a TUC-cell with erythrocyte dimensions ($r = 1.29\mu m$, $R = 2.62\mu m$ and $h = 2t = 0.81\mu m \rightarrow t = 0.405\mu m$), is computed as:

$$
\begin{aligned}
V_{TUC} =\quad & 2\pi^2 R r^2 + 2\pi \left\{ \int_0^{\sin^{-1}\frac{t}{r}} rR^2 \cos\theta - 2r^2 R \cos^2\theta + r^3 \cos^3\theta d\theta \right\} \\
=\quad & V_{torus} + 2 \left[\pi r R^2 \int_0^{\sin^{-1}\frac{t}{r}} \cos\theta d\theta \right] - 2 \left[2\pi r^2 R \int_0^{\sin^{-1}\frac{t}{r}} \cos^2\theta d\theta \right] \\
& + 2 \left[\pi r^3 \int_0^{\sin^{-1}\frac{t}{r}} \cos^3\theta d\theta \right], \quad\quad \text{(B.11)}
\end{aligned}
$$

which can be simplified to:

$$
V_{TUC} = V_{torus} + 2(A - B + C). \quad\quad \text{(B.12)}
$$

Let $x = \sin^{-1}(\frac{t}{r})$, one obtains:

$$
A = \pi r R^2 \int_0^x \cos\theta d\theta = \pi r R^2 \left. (\sin\theta) \right|_0^x \quad\quad\quad = 9.056663752, \quad\quad \text{(B.13)}
$$

$$
B = 2\pi r^2 R \int_0^x \cos^2\theta d\theta = 2\pi r^2 R \left. \left(\frac{1}{2}\theta + \frac{1}{4}\sin(2\theta) \right) \right|_0^x \quad = 8.758250701, \quad\quad \text{(B.14)}
$$

$$
C = \pi r^3 \left. \left(\frac{1}{3}(2 + \cos^2\theta)\sin\theta \right) \right|_0^x \quad\quad\quad\quad = 2.117992028 \quad\quad \text{(B.15)}
$$

and

$$
2(A - B + C) = 4.649079728. \quad\quad \text{(B.16)}
$$

Recall the volume of a torus is given by:

$$
V_{torus} = 2\pi^2 R r^2. \quad\quad \text{(B.17)}
$$

Therefore, the volume of the TUC-cell is

$$V_{TUC} = V_{torus} + 2V_{halfcyl} = 90.71088523 \mu m. \tag{B.18}$$

Appendix C

Collision Detection

In this appendix several methods for collision detection are discussed. These methods are:

1. sphere collisions,

2. randomly-oriented sphere-pack collisions,

3. flow-oriented TUC-cell collisions.

C.1   Spheres

Collision detection between spherical bounding volumes is the simplest, and fastest method to detect intersection between cells.

To test for collision between two TUC-cells with centerpoints $p_0 = (x_0, y_0, z_0)$ and $p_1 = (x_1, y_1, z_1)$, and radius $\rho = R + r = 3.91 \mu m$, on can start by computing:

$$\delta = \sqrt{(x_0 - x_1)^2 + (y_0 - y_1)^2 + (z_0 - z_1)^2}, \tag{C.1}$$

which is the distance between the centerpoints of the cells.

Bounding spheres for these cells are centered at p_0 and p_1 and have radius ρ. If these
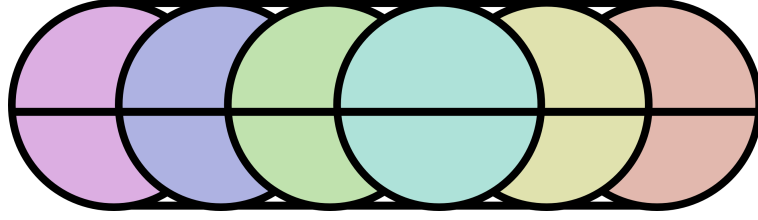
Figure C.1: Side view of a sphere pack approximation to cell shape illustrating the layout of circular plates and the sphere ring.

spheres collide, then:

$$\delta \leq 2\rho. \tag{C.2}$$

The primary advantage to using this method for collision testing is its simplicity. Additionally, this method ensures the minimum distance between any two cells is $2\rho = 2(R + r) = 7.82\mu m$.

However, this method prevents certain cellular arrangements such as rouleaus, where cells appear stacked like coins. It also wastes a large amount of space (63.8% per sphere), which means that as the number of cells increases, the harder it is to find an available space for the cell. We remark that for the hematocrit range used in our experiments this was not an issue.

C.2   Cylindrical Cell Approximation

To test for collisions between cells, approximations to their shape may be used.

We use an approximation called the "sphere-pack". A sphere-pack consists of three plates (circles in 3-space), and a ring of spheres (Fig. C.1). The top and bottom plates have radius R (the major radius of the torus), and the radius of the center plate is $\rho = R+r$, the radius of the cell. The radius of the spheres is r, which corresponds to the minor radius of the torus. The center of the shape is $C = (x_0, y_0, z_0)$, and $\vec{n} = (x, y, z)$ is the normal of the plates (a unit vector indicating shape orientation).

The center points for the spheres comprising the ring sit on the center plate. If there

are k spheres, then a sphere is placed every $\frac{2\pi}{k}$ radians. Given an orthonormal basis $\vartheta : \{\vec{n}, \vec{u}, \vec{v}\}$, where $\vec{u}$ and $\vec{v}$ are vectors on the plane, the center point of a sphere C_i is given by:

$$C_i = C + R\vec{w}, \tag{C.3}$$

where C is the center of the plane, and

$$\vec{w} = \sin\left(\frac{2\pi i}{k}\right)\vec{u} + \cos\left(\frac{2\pi i}{k}\right)\vec{v}. \tag{C.4}$$

It is important to normalize $\vec{w}$ prior to computing C_i. If $\vec{w}$ is not normalized prior to computing C_i, then there is no guarantee that C_i will sit on the edge of the center plate.

C.2.1 Intersection Testing

Detection of intersection between two sphere-packs consists of three parts:

1. plate-plate intersection

2. sphere-sphere intersection

3. plate-sphere intersection

Plate-Plate Intersection

Let $x \circ y$ represent the dot product of vectors x and y. And let C_a and C_b be the center points of plates a and b respectively. Recall that a plate is a circular region of a plane.

A plane is defined by the equation [19]:

$$a_0 x + a_1 y + a_2 z + \alpha = 0, \tag{C.5}$$

which we can expressed as:

$$\vec{n} \circ C = \alpha, \tag{C.6}$$

where $\vec{n}$ is the plane's normal, and C is a point on the plane.

Given two planes $\vec{n}_a \circ C_a = \alpha_a$, and $\vec{n}_b \circ C_b = \alpha_b$ the line of intersection is:

$$\vec{l} = \vec{n}_a \times \vec{n}_b. \tag{C.7}$$

If $\vec{l}$ has magnitude 0, then the planes are parallel and therefore they do not intersect (or are coincident). If planes are coincident, then intersection will be caught by sphere-sphere testing, therefore the case of coincident planes is ignored.

The next step involves finding a point p coincident with both planes and $\vec{l}$ by solving the system of equations:

$$\vec{n}_a \circ p = \alpha_a \tag{C.8}$$

$$\vec{n}_b \circ p = \alpha_b, \tag{C.9}$$

yielding the line $m = p + s\vec{l}$, which represents the intersection of the planes.

One then needs to find the shortest distance from plate centers (C_a, and C_b) to the line $m = p + s\vec{l}$. The shortest distance is found by first finding s (assuming $\vec{l}$ is a unit vector):

$$s = \vec{l} \circ (C_a - p), \tag{C.10}$$

then computing the distance δ_{line} as:

$$\delta_{line} = \left| C_a - (p + s\vec{l}) \right|. \tag{C.11}$$

If the circle centered at C_a, with radius r_a sitting on plane a intersects the circle centered at C_b, with radius r_b sitting on plane b then first, the line m must be coincident which is true if:

$$\delta_{line_a} = \left| C_a - (p + s_a\vec{l}) \right| \leq r_a, \tag{C.12}$$

and

$$\delta_{line_b} = \left| C_b - (p + s_b \vec{l}) \right| \leq r_b. \tag{C.13}$$

Then, if the distance between

$$\left| (p + s_a \vec{l}) - (p + s_b \vec{l}) \right| \leq r_a + r_b, \tag{C.14}$$

the circles intersect.

Sphere-Sphere Intersection

This is described in Appendix B.

Plate-Sphere Intersection

Given a sphere with center C_s and radius r, and a plane $\vec{n} \circ p = \alpha$ (recall from Section C.2.1), the distance between C_s and the plane is:

$$\delta_{plane} = |\vec{n} \circ C_s - \alpha|, \tag{C.15}$$

assuming $\vec{n}$ is a unit vector. If $\delta_{plane} \leq r$, the sphere intersects the plane.

To find the point q where the line through C_s with direction $\vec{n}$ intersects plane $\prod$, compute:

$$s = \alpha - (\vec{n} \circ C_s), \tag{C.16}$$

assuming $\vec{n}$ is a unit vector. Then point $q = C_s + s\vec{n}$ is a point on the plane.

If the sphere intersects the plane, the region of intersection forms a circle whose radius $0 \leq r_0 \leq r$. The radius r_0 is computed as:

$$r_0 = \sqrt{r^2 - \delta_{plane}^2}. \tag{C.17}$$

The circular plate on the plane is centered at p and has radius R. If the circle centered at q with radius r_0 intersects the plate, then:

$$|p - q| \leq (R + r_0), \tag{C.18}$$

and therefore the sphere intersects the circular plate.

C.2.2 Collision Detection Shortcut for Flow-Oriented Cells

The plane of a flow-oriented TUC-cell is parallel to the xy-plane. A quick intersection test for this orientation is to first check if the bounding spheres intersect. If the bounding spheres intersect, the cells intersect if:

$$|z_0 - z_1| \leq 2r, \tag{C.19}$$

where r is the minor radius of the torus, and z_0, z_1 are the z-coordinates of the cell center points.

Appendix D

CUDA Implementation Considerations

This appendix provides an implementation overview of the proposed framework for CUDA (a massively multi-threaded platform).

D.1 Embarrasingly Parrallel Algorithms

The proposed sieve factor estimation framework presented in this thesis is a stochastic algorithm, with each repetition identical and independent of the others. Algorithms with these properties lend themselves to parallelization with little difficultly. Likewise, they are often referred to as "embarrasingly parallel" [8].

D.2 CUDA Specifications and Machine Setup

The sieve framework presented in this thesis was implemeted with the CUDA 2.0 platform for Linux. The maximum number of threads per block is 128, and the maximum number of blocks per grid is 128 (a maximum of 16384 threads per function call) [10]. These values were selected to maximize performance while avoiding the limitations of the Graphics

Processing Unit (GPU) used (GeForce 88000M GTX).

D.3 Implementation Details

The proposed framework for the estimation of the sieve effect factor can be divided into two parts: cell generation/distribution, and sieve test.

D.3.1 Cell Generation/Distribution

A cell is generated randomly as two points: the center $C = (x, y, z)$ and the orientation $\theta = (\theta_x, \theta_y, \theta_z)$. To determine if a cell C_i is valid[1], collision testing is performed between C_i and C_j for all $j \neq i$. Since collision tests are independent[2], this portion of the algorithm can be pushed onto the GPU.

The centerpoints and orientations of all generated cells is copied to the GPU's global memory space. One thread is created for each already-generated cell, and each thread tests for collision between C_i and one other cell (*i.e.*, thread 0 tests for collision between C_i and C_0, and thread j tests for collision between C_i and C_j). If a collision occurs, a counter is incremented.

Since access to the collision counter must be protected[3], each thread is given its own collision counter. After all threads have completed, the collision counters (array) is copied from the GPU to the CPU, and summed. If the sum of counters is zero, the cell defined by C_i and θ_i is valid and generation continues. Otherwise, the process is repeated until a valid cell is found.

---

[1]A valid cell is one that does not collide with existing cells.
[2]Testing for a collision between C_i and C_j is independent of C_i and C_{j+1}.
[3]Only one thread can attempt a write at a time.

D.3.2 Sieve Test

The sieve test computes the number of intersections between a ray v and the generated cells C. These intersection tests are independent, like the algorithm in Section D.3.1. Therefore, they are pushed onto the GPU.

The centerpoints and orientations of all cells is copied into the GPU's global memory space. One thread is created for each cell, and each thread tests for intersection of the ray v with one cell (*i.e.*, thread 0 tests for intersection of v with C_0, thread j tests for intersection of v and C_j, etc.). Each thread is given its own counter (as in Section D.3.1) and the intersection results are summed by the CPU after all threads have completed. This sum represents the number of intersections between the ray v and the cells, and it is used to compute the sieve effect factor.

Appendix E

Supplementary Results

This appendix presents results which detail the effects of certain implementation decisions on the estimation of sieve effect factor.

E.1 Iterations to Achieve Convergence of Results

The ray casting framework presented in this thesis is based on a stochastic algorithm. To find asymptoticaly convergent results (Section 3.6), many iterations are performed.

We selected $N = 10000$ as the number of iterations to execute, because it balances accuracy with execution time. Figures E.1 and E.2 illustrate the how the number of iterations affects both the sieve effect value and execution time. Note that while $N = 100000$ produces as slightly smoother sieve effect curve, the execution time is $10\times$ higher than $N = 10000$.

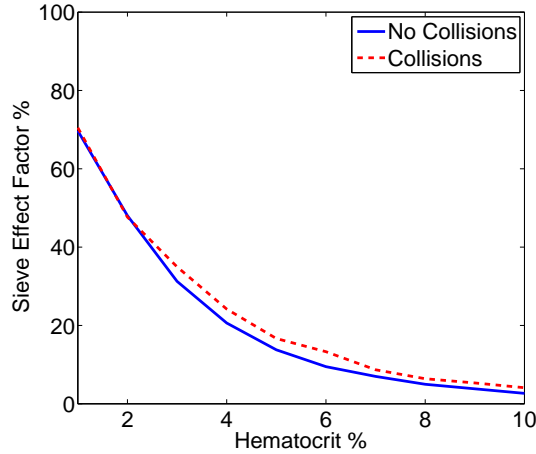## E.2 Effect of Collision Detection on Sieve Effect

Red blood cells cannot overlap in *in vivo* or *in vitro* blood samples, but this is possible for *in silico* simulations where cells are not physical objects, but numbers. In the ray casting framework presented in this thesis, collision detection is used to prevent overlap. However,
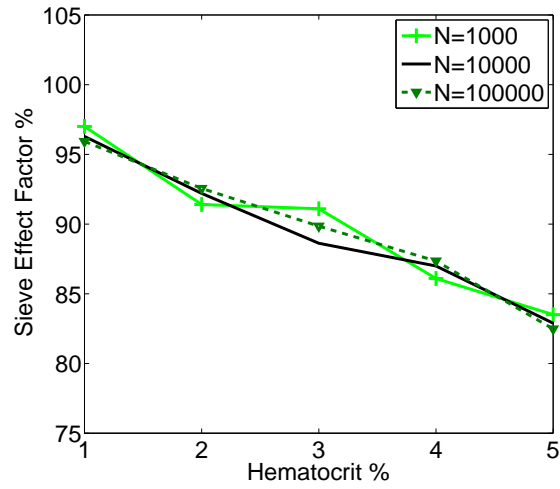
Figure E.1: The effect of iterations on the computation of the sieve effect factor. A $0.01mm$ sample of randomly-oriented TUC-cells is used in this experiment.
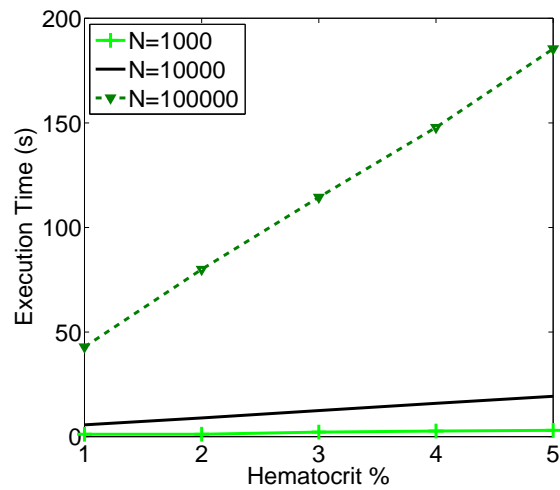
Figure E.2: Execution time versus hematocrit. A $0.01mm$ sample of randomly-oriented TUC-cells is used in this experiment.
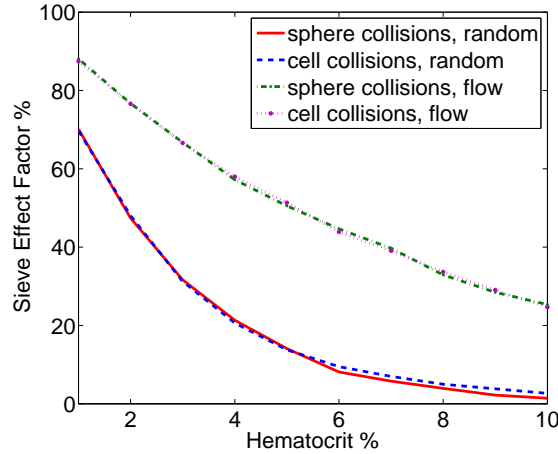
Figure E.3: The effect of collision detection on the computation of the sieve effect factor. A 0.1mm sample of randomly-oriented TUC-cells is used in this experiment.

collision detectection increases execution time. Therefore, an experiment was conducted to determine the effect of collision detection on the sieve effect factor.

When collisions occur, the total volume occupied by the cells is reduced (lower hematocrit). We observed that lower hematocrits have higher sieve effect factors, likewise we expected that collisions would also increase the factor. Figure E.3 illustrates the effects of collisions on the sieve effect factor. Lower hematocrits correspond to fewer cells and a lower probability of a cell collision, thus the difference in sieve effect factor is small. As hematocrit increases, the number of cells also increases, which, in turn, increases the probability of cell collisions. This behaviour can be observed in the plot presented in Figure E.3.

E.2.1 Spherical versus Approximated Collision Detection

Two methods of collision detection were discussed in Appendix B, spherical and cylindrical-approximation. Bounding spheres is the simplest form of collision testing, but they prevent the formation of rouleaus by enforcing a minimum distance between cells: cylindrical-approximation collision testing does not prevent the formation of rouleaus. This subtle difference in distribution may affect the sieve effect factor, therefore an experiment was

Figure E.4: The effect of different collision detection algorithms on the computation of the sieve effect factor. A $0.1mm$ sample of randomly-oriented, and flow-oriented TUC-cells are used in this experiment.

conducted to quantify it.

The experiment generates $0.1mm$ samples of random and flow-oriented TUC-cells using spherical collision testing and cellular collision testing. Then, the sieve effect factor is computed for these samples and compared.

The collision detection algorithms were found to have no influence on sieve effect factor for hematocrit less than 5%. However, beyond $H = 5\%$ it can be observed in Figure E.4 that spherical collision testing produces slightly higher values for the sieve factor.

E.3 Methods of Iteration

The stochastic framework for computing the sieve effect factor can execute repetitions in a variety of ways. One is to generate a unique blood sample for each iteration, another is to use a unique ray position, and a third uses a combination of the previous ideas. This section details the effects of these iteration techniques on the estimation of seive effect.

E.3.1 Unique Sample Iteration

The unique sample iteration technique generates a new blood sample for each iteration and holds the position of the ray constant. It ensures iterations are independent, and therefore this technique is considered the most accurate implementation. However, the generation of a new sample for each ray is costly, which causes this technique to be the slowest of all those tested.

E.3.2 Unique Ray Iteration

The unique ray iteration generates a new ray position for each iteration and uses only one blood sample. This technique does not guarantee that iterations are independent (as it is possible for rays to be near each other and therefore intersect the same cells). However, this technique is the fastest of all tested techniques.

E.3.3 Hybrid Iteration

The hybrid iteration technique generates a new ray position for each iteration and uses unique blood samples. Specifically, if N iterations are performed then $N/1000$ unique blood samples are generated. This technique provides a greater level of independence than the unique ray technique. Performance wise, it is faster than the unique sample technique but slower than the unique ray technique.

E.3.4 Iteration Results

Prior to the selection of an iteration technique, an experiment was conducted to determine the effects of these techniques on the computation of sieve effect factor. The results of this experiment are shown in Figure E.5. Note that the unique sample and hybrid iteration techniques produce similar results for all hematocrit. However, the unique ray iteration technique produces results which decrease faster (as hematocrit increases) than the other
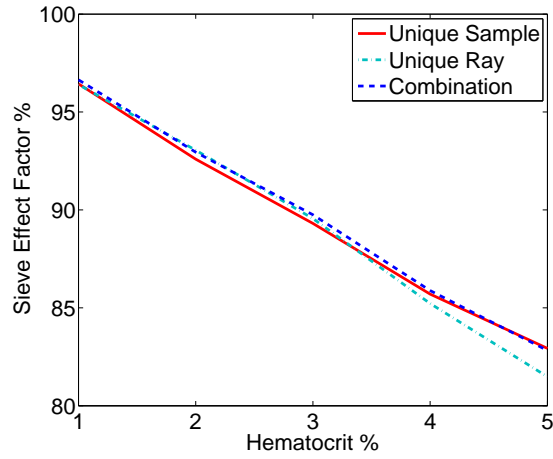
Figure E.5: The effect of different iteration techniques on the computation of the sieve effect factor. A $0.01mm$ sample of randomly-oriented TUC-cells is used in this experiment.

iteration techniques.

The results presented in the main thesis body were obtained using the hybrid iteration technique. This choice was motivated by the fact that hybrid iteration technique results agree with the results provided by the unique sample technique, while exhibiting a faster execution time.